

# Experimental Characterization of a Small Scale Arc-Jet Flow Using a Spatially Resolved UV-nIR Spectroscopy System

Maily T. B. Buquet\*, Eric Won Keun Chang†, Benjamin A. O. Williams‡ and Tobias A. Hermann §,  
*University of Oxford, Southwell Building, Osney Mead, OX2 0ES Oxford, UK.*

This paper presents emission spectroscopy measurements of the OPG2 plasma generator, a small scale thermal arc-jet recently upgraded to transition from argon to nitrogen and air flows. Spectra were recorded between 200 nm and 900 nm using a spatially resolved spectroscopy system currently under development at the Oxford Thermofluids Institute, of which design and characterisation are provided in this work. After calibration, the spectra were band-fitted to a range of radiative emission simulations of different temperature profiles and species population densities, assuming a chemical equilibrium composition. Translational and vibrational temperatures of the flow over 60 mm from the nozzle exit were inferred by identifying the closest match through a least-square fitting routine at six discrete locations. Radial enthalpy profiles were obtained under the assumption of fully developed turbulent free-jet, and the diameter of the jet was initially considered as the diameter of the visibly radiating gas, and later adjusted to include non-radiative species at temperatures above ambient. For operating conditions of 250 A and 0.2 g.s<sup>-1</sup>, nitrogen flow was found to have a rotational temperature  $T_r$  varying from 5200 K at the nozzle to 2800 K 60 mm downstream, and vibrational temperature  $T_v$  varying from 8300 K to 2900 K. For the same operating conditions with air as the test gas,  $T_r$  varied from 7200 K at the nozzle to 3100 K 60 mm downstream, and  $T_v$  from 9300 K to 3000 K.

## I. Nomenclature

### A. Acronyms

$nIR$  = Near infrared  
 $Vis$  = Visible  
 $VUV$  = Vacuum ultraviolet

### B. Symbols

$h$  = Enthalpy  
 $I$  = Radiance intensity  
 $N_2$  = Nitrogen  
 $R$  = Jet local radius  
 $r$  = Jet radial location  
 $T_t$  = Translational temperature  
 $T_r$  = Rotational temperature  
 $T_v$  = Vibrational temperature  
 $T_e$  = Electronic temperature  
 $\lambda$  = Wavelength

\*DPhil Student, University of Oxford, Oxford Thermofluids Institute, United Kingdom

†Postdoctoral Research Assistant, University of Oxford, Oxford Thermofluids Institute, United Kingdom

‡Associate Professor in Thermofluids, University of Oxford, Oxford Thermofluids Institute, United Kingdom

§Departmental Lecturer, University of Oxford, Oxford Thermofluids Institute, United Kingdom

## II. Introduction

During atmospheric re-entry, space vehicles interact with the gas molecules constituting the atmosphere. The spacecraft's high kinetic energy is converted to internal energy of the surrounding gas particles through a bow shock that forms in front of the vehicle. The shock layer in front of the spacecraft presents a sudden increase of temperature, leading to significant heat fluxes to the surface. For speeds as high as  $15 \text{ km.s}^{-1}$  (typical of a Mars return trajectory), radiative heating becomes the primary source of heat load to the vehicles [1], by far dominant over convective heat transfer [2]. Ablation-radiation coupling in the flow field near the surface impacts chemical and thermal fields, inducing further complexities to the prediction of species concentration and surface temperatures. Plasma facilities recreate the high-enthalpy flow conditions encountered during re-entry in ground test facilities [3]. They can be used to test diverse materials and geometries, generating valuable data for spacecraft thermal protection design. Plasma facilities offer steady test conditions enabling investigation of these processes through the use of various diagnostics such as emission spectroscopy and high-speed imaging [4–6], which allow to study the complex molecular processes stemming from the ablative material interaction with the surrounding gas.

Spectroscopy systems present no physical boundary with the gas or model, in contrast to other intrusive diagnostics which can potentially alter the flow field structures or the gas chemistry. Spectra can be used to understand the coupling between material ablation, surrounding gas and (re)radiation to the test model. Near the facility nozzle, spectra can be used to characterize the plasma generated by the arc-jet and identify the state of the flow interacting with the model. Characterization of freestream test conditions is crucial to understand the impact of the different flow parameters on the surface chemistry and heat loads. Experimental data is valuable to achieve better modelling by providing boundary conditions for numerical simulations. Additionally, this allows a better understanding of the experimental set-up testing range as well as its test-to-test repeatability.

The spatially resolved spectroscopy system discussed in this paper is used to investigate the flow fields generated in the OPG2 facility at the University of Oxford. Design of the new plasma generator and additional testing are presented in sister papers [7–9]. Emission spectroscopy from the nIR to UV is performed to obtain  $N_2$  and air spectra over 60 mm from the nozzle exit. The spectra are calibrated in all three dimensions of wavelength, space and spectral radiance. Simulations of equilibrium chemistry and spectral radiance are performed for various flow enthalpies using the NASA programs CEA (Chemical Equilibrium with Applications) and NEQAIR (Nonequilibrium Radiative Transport and Spectra Program). The experimental data is band-fitted to the range of simulations [10] to infer rotational and vibrational temperatures evolutions of the plasma flow at different distances from the nozzle exit. This work focuses on the characterisation of the newly developed plasma flow conditions under fully developed turbulent free-jet assumption, and presents the experimental arrangement of the spectroscopic system and its integration to OPG2, the design and characterisation of the optical system, and the calibration and analysis of the spectra obtained under various assumptions. Final results of spatial temperatures evolution for  $N_2$  and air flows are shown.

## III. Experimental Arrangement

The Osney Plasma Generator 2 (OPG2) facility is a thermal arc-jet facility which can be used as a stand-alone plasma generator for material testing [8], and is designed to be integrated to expansion tube facilities for model pre-heating in hypervelocity flows [11]. This paper focuses on the characterisation of the arc-jet as a plasma generator by means of emission spectroscopy. In this work, the optical set-up is adapted to capture UV-nIR spatially-resolved spectra of the OPG2 flows after its upgrade to transition from argon to  $N_2$  and air flows.

### A. Osney Plasma Generator 2 (OPG2)

#### 1. Layout

The 21.5 kW thermal arc-jet is located in a 20" diameter stainless steel vacuum chamber. Picture and schematic views of the system can be seen in Figs 1 and 2. Plasma is initially generated by heating argon gas using the electric arc generated between the tungsten cathode of an industrial welding torch and a copper nozzle. The mass flow rate is in the order of  $0.2 \text{ g.s}^{-1}$  and is controlled by a mass flow controller located downstream of the pressure regulator mounted to the gas bottle. The system capability was recently upgraded to work using different gases [8]. Once the argon plasma flow is stable, nitrogen is introduced and argon gradually cut off until the flow consists of purely nitrogen. Oxygen is finally added to obtain a synthetic air mixture. The gas mixture is expanded through a Laval nozzle and reaches the test model mounted in the chamber for material testing. An exhaust line behind the model allows to retrieve ablation products and condenses them in a heat exchanger in order to keep the chamber relatively pure and control its pressure.

The system is equipped with various sensors measuring pressure and temperature in the nozzle, the chamber and the model, and its operation is controlled and recorded by a National Instruments CDAQ data acquisition system. Water cooling lines ensure that the system's material stays under critical temperatures. Nozzle temperatures, mass flow, heat loss due to cooling of the anode and stagnation chamber and vessel pressures are recorded during the runs to monitor that the system is operating within its design range.

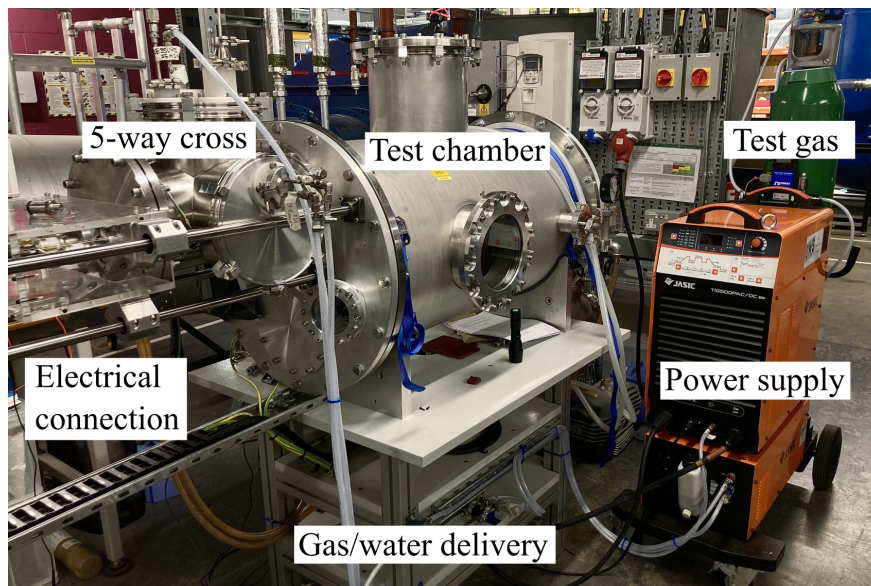


**Fig. 1 OPG2 plasma generator system [7].**

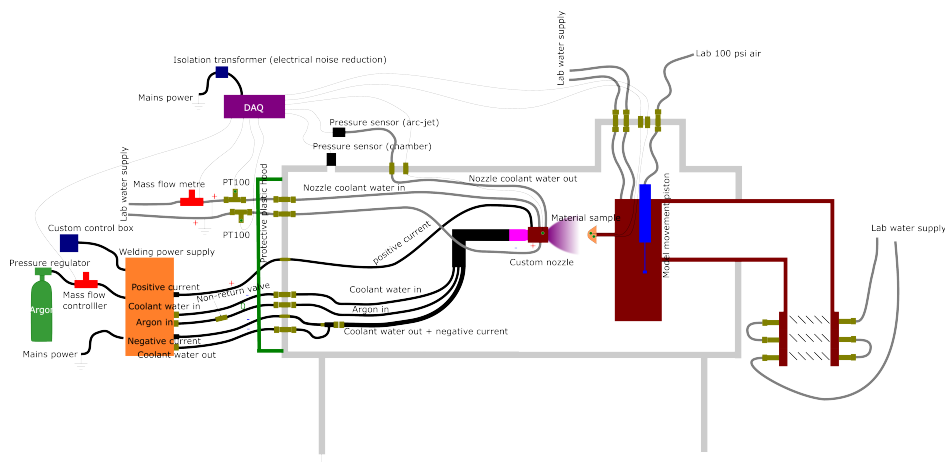


**Fig. 2 Schematic overview of the OPG2 plasma generator system [12].**

## 2. Diagnostics

The chamber is equipped with five window inserts to set-up different diagnostics during material testing. An Optris P1 M infrared camera and embedded thermocouples track sample material temperature during the duration of the run. A Photron FASTCAM Mini UX100 high-speed camera is mounted above the test section to observe overall behaviour of the plasma and sudden high-frequency changes. Point emission spectra are obtained in the vis-nIR by a Thorlabs CCS200M fibre-coupled spectrometer, and between 200 and 900 nm by a McPherson Model 634 spectrometer to obtain spatially resolved spectra. The latter measurements are the focus of this work.

## B. Spectroscopy System Layout

The spectroscopy system is designed to be a versatile set-up able to be mounted onto various facilities as well as being operated alone in a bench-top configuration for calibration purposes. Originally designed to investigate VUV emission and UV-vis absorption spectra of T6 Stalker Tunnel shock tube flows [13], the optics can be mounted into vacuum chambers and the spectrometer and camera fully evacuated in the configuration shown in Fig 3a. The optical system is placed on a table of adjustable height which is mounted on wheels, and can be fitted with different inserts to fit a range of facilities. This work presents vis-nIR spectra obtained with the optical configuration shown in Fig 3b, designed to fit the OPG test chamber arrangement, as detailed in Section IV. The current state of the set-up can be seen in Fig 4.

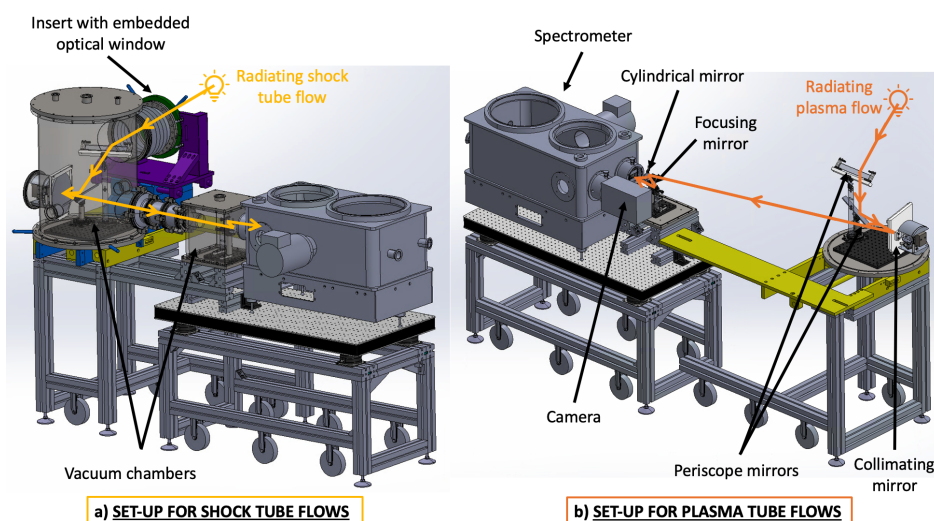


**Fig. 3** CAD overview of the spectroscopy system. Light path between mirrors is also shown in Fig 4 and in ray-tracing simulations in Fig 5.

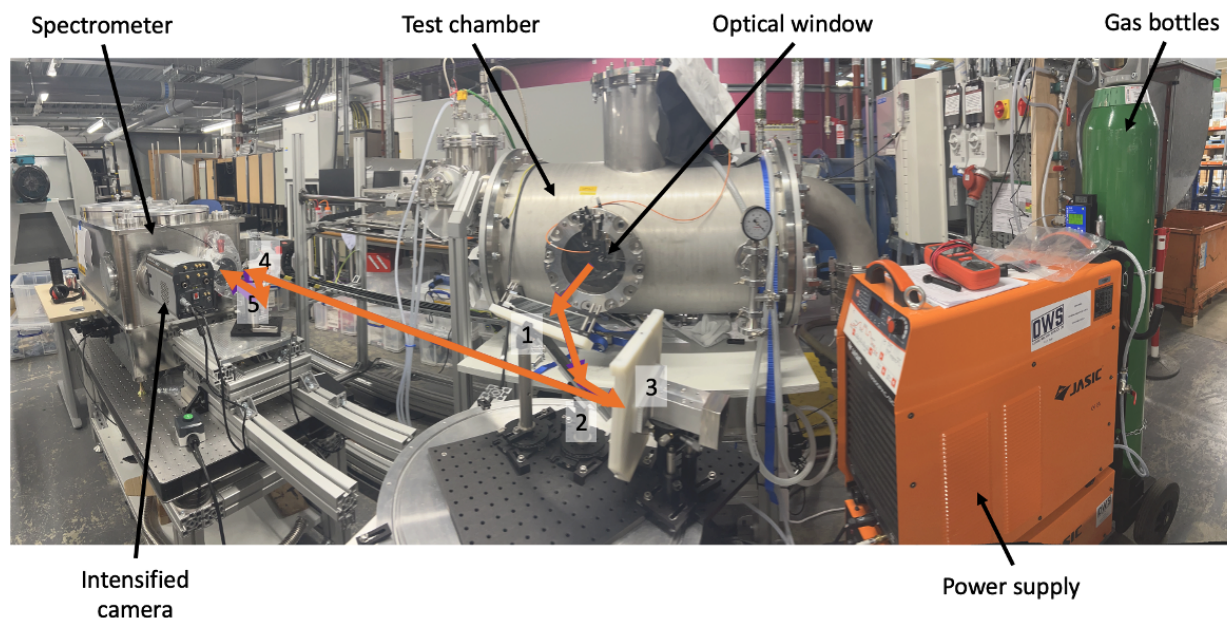


**Fig. 4** Spectroscopy set-up used in this work. Light path from the test section of OPG2 through the five mirrors and onto the spectrometer slit is shown in orange.



## IV. Experimental Design and Characterisation

The optical system presented in this work uses a set of five mirrors to redirect the light from the centreline of the test section to a high spectral resolution McPherson 207V Spectrograph on which an intensified P43 iStar sCMOS camera is mounted. To reduce spatial blur and obtain the highest fidelity and intensity of signal, the collection optics were designed in a telecentric configuration as it was experimentally found that telescopic systems suffer from larger spatial blur due to ray divergence [14].

### 1. Design

Ray tracing simulations were performed to widely characterise the system in the design stage using the Optometrika MATLAB library [15]. An example simulation is shown in Fig 5, where the light rays from three sources located at the nominal centreline of the OPG2 test section travel through the window and get successfully collimated by the collimating mirror.

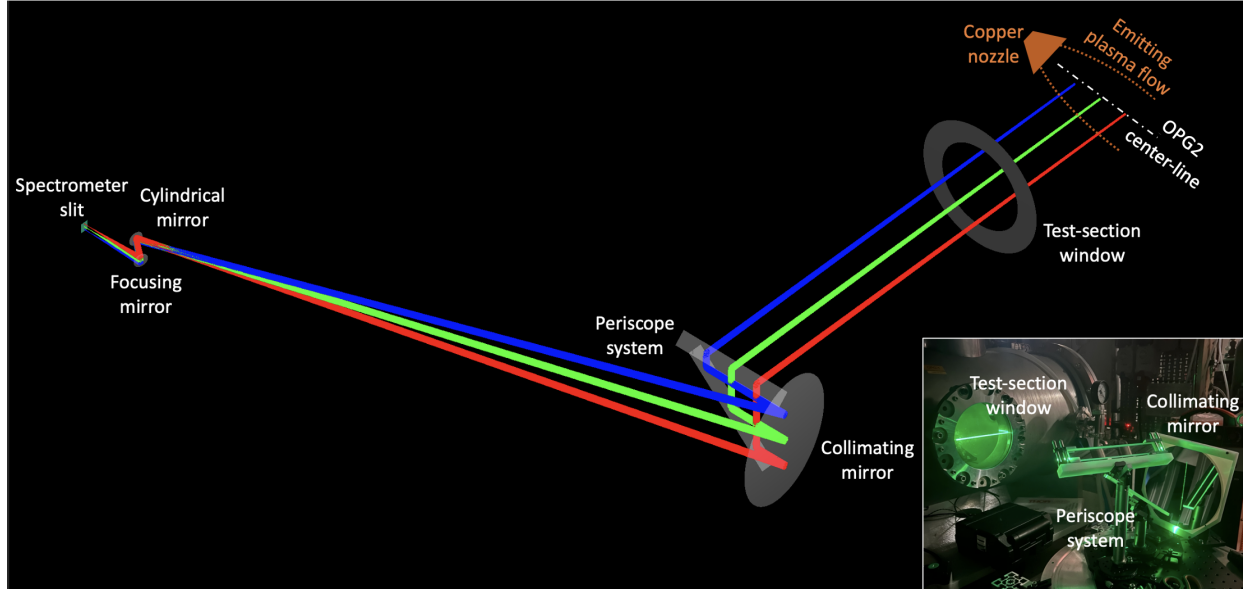


**Fig. 5** Ray-tracing simulations using Optometrika [15] for three light sources emanating from the OPG2 test section centreline.

By simulating the camera sensor at the location of the spectrometer slit, optical aberrations due to astigmatism were quantified and corrected using a cylindrical mirror further upstream. The signal received by each pixel of the simulated sensor was plotted and is shown in Fig 6. In Fig 6a, before the introduction of a cylindrical mirror, the image of the circular object simulated in the test section is distorted in space. This phenomenon was indeed observed experimentally during alignment of the set-up by recording the signal just upstream of the cylindrical mirror. The integration of the cylindrical mirror focuses the rays at the same location in both planes, and helps to recover shape and magnification as shown in Fig 6b.

These simulations were also used to confirm the expected magnification calculated from Gaussian optics theory, defined as the ratio of the focal lengths of the powered mirrors  $M = \frac{f_{\text{collimating}}}{f_{\text{focusing}}}$  for a telecentric system. Expected magnification from Gaussian optics theory is  $M_{\text{Gauss}} = 7.18$ , slightly below the magnification  $M_{\text{sim}} = 7.84$  found through simulation and shown by the red arrow in Fig 6b. By placing an array of light sources separated by known distances on the centreline of the test section, magnification was experimentally measured as  $M_{\text{exp}} = 7.93$ , close to the predicted value.

Two light sources (in blue and red in Fig 5) were simulated originating from both edges of the test section window to estimate the field of view. Simulated field of view shown by the yellow arrow in Fig 6b spans 136 mm along the test section window, which was experimentally confirmed using the same method as for magnification measurement. About 60 mm were usable for flow radiation acquisition during OPG2 runs, as the first third of the image was showing the nozzle and the last 30 mm suffered from too much spatial smearing to obtain resolvable signal.

To simplify the alignment process, the mirrors are positioned such that the light beam leaving the collimating mirror travels along a plane parallel to the slit of the spectrometer. The cylindrical and focusing mirrors can be used at nominally equal angles to redirect the light onto the slit, and adjustments are made using the collimating mirror only. As the light path between collimating and cylindrical mirrors is particularly long, it was easier to observe and correct angle errors such that the light entered the spectrometer in a plane parallel to the slit to avoid stray light inside the spectrometer.

The long light path was also used to confirm the telecentricity of the optics by measuring the beam's height at various points along the path to make sure it stayed constant. This required the use of the periscope mirrors at an angle, as can be seen in the bottom right corner of Fig 5. A laser level was used to ensure the periscope turns the light by  $45^\circ$ .

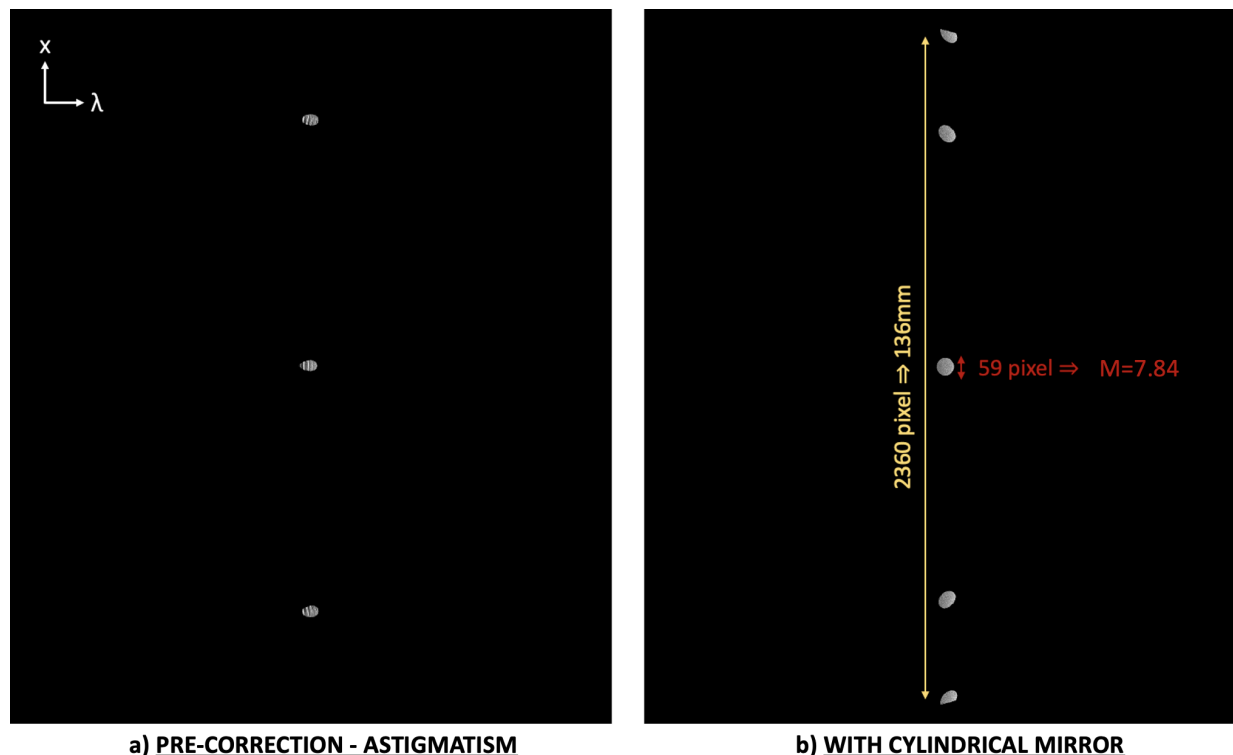


**Fig. 6 Simulations of light rays received by the camera sensor from light source objects located at the test section centreline such as shown in Fig 5.**

## 2. Calibration

The raw images obtained need to be post-processed in all dimensions of wavelength ( $\lambda$ ), space ( $y$ ) and spectral radiance ( $I$ ) by calibrating the system. A wavelength calibration was performed by fitting easily identifiable atomic lines from an IntelliCal mercury ( $Hg$ ) and neon-argon ( $Ne - Ar$ ) calibration source to their expected wavelengths. The fitted wavelength axis is subsequently used to obtain the Spectral Instrument Line Shape (ILS) by fitting the most intense spectral line measured to the square-root of a Voigt profile, the most accurate shape function to capture the ILS with an intensified CCD array [16], as shown on the left side of Fig 7. The experimentally measured full-width half-maximum parameters of 0.86 nm and 0.01 nm for Gaussian and Lorentzian profiles respectively were used to artificially broaden the simulated spectral lines in Section VI before comparison with their experimental counterparts.

The spatial calibration was achieved in a similar way, by taking images of light sources located at known distances from the nozzle exit along the test section's centreline. Each pixel on the image is then attributed a spatial location, i.e a distance from the nozzle exit. The spatial axis is then used to obtain a spatially variable spatial smearing function. This function represents the merging of optical information due to ray divergence prior to their collimation, and collection optics and CCD array resolution. Spatial smearing was measured using a knife edge placed in front of an integrating sphere at the centreline of the test-section. Images were recorded at different locations along

the field of view to obtain edge spread functions (ESF) and resolve spatial smearing in space. The line spread function (LSF) is obtained by taking the derivative of the ESF, i.e by measuring how far from an ideal-system's Dirac impulse function the signal deviates. The LSF is a good indication of signal intensity loss and spatial smearing of information, and dictates the practical spatial resolution limit of the optical system. The experimentally measured full-width half-maximum parameters varied from 0.556 to 1.75 mm for Gaussian and 0.008 and 0.210 mm for Lorentzian profiles, with averages of 0.8362 and 0.0575 mm. An example of LSF fitting is shown on the right side of Fig 7.

Finally, spectral radiance was calibrated in situ using an integrating sphere to obtain a wavelength dependant conversion of radiance per count. Calibration images were acquired for each combination of spectrometer centre wavelength and camera gain used during experiments. The radiance calibration curve provided by the manufacturer for this specific source was interpolated in wavelength to get a value of spectral radiance at each pixel of the sensor. The ratio of integrating sphere radiance values to counts measured at each wavelength location provides a wavelength dependant count to radiance conversion function. After normalising experimental images by their integration times, the correct conversion was applied for corresponding gain.

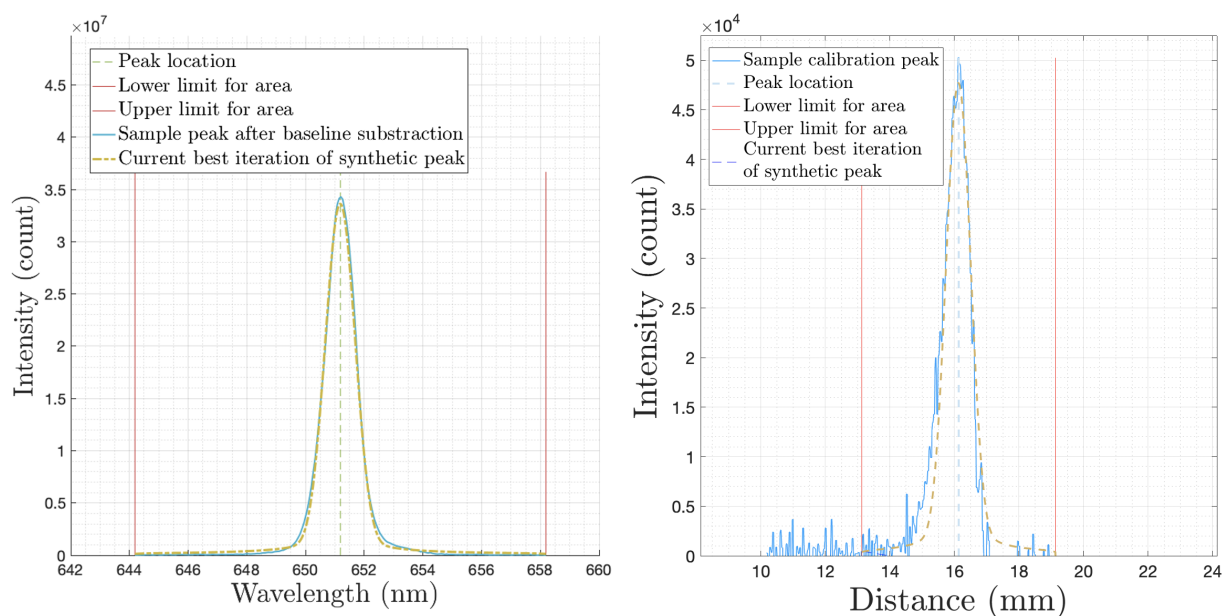


**Fig. 7 ILS (left) and LSF (right) fitting for the optical system.**

## V. Experimental Procedure and Analysis

The spectroscopy system described in Section III.B is focused on the centreline of the OPG2 plasma generator during a run to obtain spatially resolved emission spectra spanning a field of view of approximately 60 mm downstream of the nozzle. Spectra were obtained for nitrogen and air at four spectrometer center wavelength locations during each run: 800 nm, 650 nm, 400 nm and 250 nm. For measurements at 650 nm and 800 nm, a long pass filter was placed at the spectrometer slit to filter out higher order lines from wavelengths below 395 nm. The data shown in this paper focuses on a 250 A arc-current and 0.2 g.s<sup>-1</sup> mass flow rate. Spectra were taken when pressure in the chamber was plateau-ing, although it is believed that the conditions were not completely stable and suffered from temporal fluctuations, notably due to a build up of back pressure in the chamber.

The data acquired using the spectroscopy system is used to infer temperatures of the core flow by comparison with radiative spectra simulations generated with NEQAIR. Simulations are generated for a range of rotational and vibrational temperature combinations. Each simulation is then fitted to an experimental spectra through a least-square routine, and the best fit is used to infer temperatures.

### A. Temperature profile assumption

Enthalpy profiles of the jet are obtained from semi-empirical law for fully developed nitrogen turbulent free-jet [17]:

$$h_r = h_{max} \left( 1 - \left( \frac{r}{R} \right)^{\frac{3}{2}} \right)^3 + h_{ambient} \quad (1)$$

where  $h_r$  is radial enthalpy,  $h_{max}$  maximum enthalpy,  $r$  radial location,  $R$  local jet radius, and  $h_{ambient}$  ambient enthalpy. Maximum enthalpy  $h_{max}$  was initially calculated from the jet power and mass flow rate, but judged unsatisfactory due to errors in mass flow rates recorded during experiments. A range of maximum temperatures  $T_{max}$  was assumed and their corresponding  $h_{max}$  at equilibrium calculated from CEA simulations. The field of view was discretised in 6 spatial locations with origin at the exit of the nozzle, and local jet radius  $R$  was estimated at each point as explained in Section V.B. All 6 spatial locations were then attributed a range of enthalpy profiles  $h_r$  matching their local jet radius  $R$  by feeding an array of maximum enthalpies  $h_{max}$  into Equation 1. CEA simulations were conducted to retrieve enthalpies as a function of equilibrium temperatures ranging from  $T_{ambient}$  to the largest  $T_{max}$  assumed, by 100 K increments. By interpolating the enthalpies to match all values in the enthalpy profiles, temperature profiles could be generated for each locations, as shown in Fig 8. These temperature profiles were used to run NEQAIR spectral radiance simulations assuming a 2-temperature model ( $T_t = T_r \neq T_v = T_e$ ), such that to each  $T_r$  profile generated from an initial  $T_{r,max}$ , 17 corresponding  $T_v$  profiles were paired using different  $T_{v,max}$ .

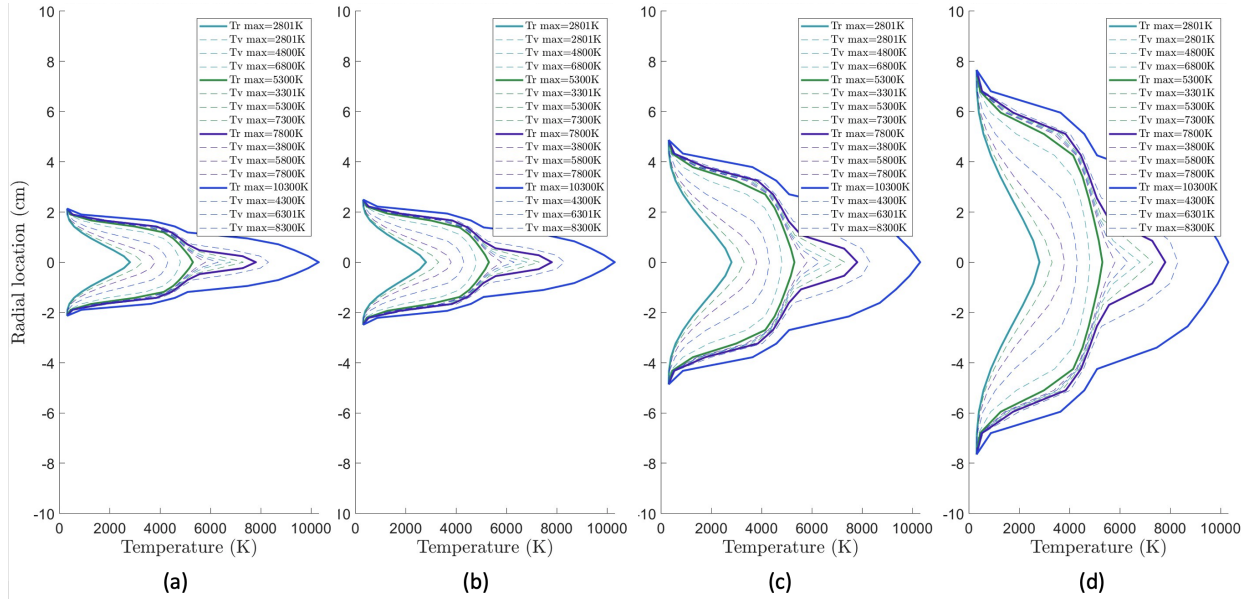


**Fig. 8** Temperature profile combinations subsets at different locations from the nozzle exit: a) 0 mm b) 30 mm c) 60 mm d) 90 mm.

### B. Jet diameter

Jet radii  $R$  were estimated at different locations spanning 60 mm from the nozzle exit. As first approximation, this was done by measuring the radius of the visibly radiating gas  $R_{vis}$  using high speed imaging. Initial estimations varied from  $R_{vis} = 1.5 \text{ cm}$  at the nozzle exit to  $R_{vis} = 5 \text{ cm}$  90 mm downstream. These diameters were later increased to account for non-radiating species as described in the following.

NEQAIR simulations were ran between 300 and 780 nm at different temperatures above ambient to define a range which although not generating visibly radiating chemistry, are above ambient and should therefore be considered part of the jet. The temperature of the simulated spectra for which peak radiance in the visible was equal to 10% of the peak spectral radiance of the simulation best fitted to experimental spectra was chosen as initial threshold and defined as  $T_{rad,vis} = 4200 \text{ K}$ , i.e. the temperature above which radiance intensity in the visible becomes strong enough to be observed, matching  $R_{vis}$ . Once this threshold temperature was defined, temperature profiles as calculated in Section V.A had to be updated. The jet radius  $R$  was increased by steps and fitted to new temperature profiles using the routine



of Section V.A until the radial location  $r$  where  $T_r = T_{rad,vis}$  corresponded to the observed radius of radiating jet  $R_{vis}$ . This method led to an increase of  $R$  of about 94%, and a different approach was taken to estimate  $T_{rad,vis}$  more conservatively. The spectral radiance of all simulations was integrated over wavelength in the visible to obtain total radiance as a function of  $T_v$  and  $T_r$ . Their derivatives with respect to both variables were plotted to identify the temperatures for which radiance would suddenly spike, creating a visible sudden contrast of observed radiance in the visible, assumed to be the visible edge of the plume  $R_{vis}$ .  $T_{rad,vis}$  was updated to 2300 K, as this is the temperature for which Fig 9 shows a sudden step in radiance gradient. This decrease in estimated  $T_{rad,vis}$  was judged more conservative, as temporal fluctuations of radiance may lead to an observed  $R_{vis}$  slightly higher than the actual time-averaged radius visibly radiating, due to the exponential relationship between temperature and radiative emission.  $T_{rad,vis} = 2300$  K was chosen as a starting point, and spectral radiance simulations were updated for the new optical depth. The whole procedure was repeated until radial profiles reached a plateau, with a jet radius overall increased by about 88% from initial values.

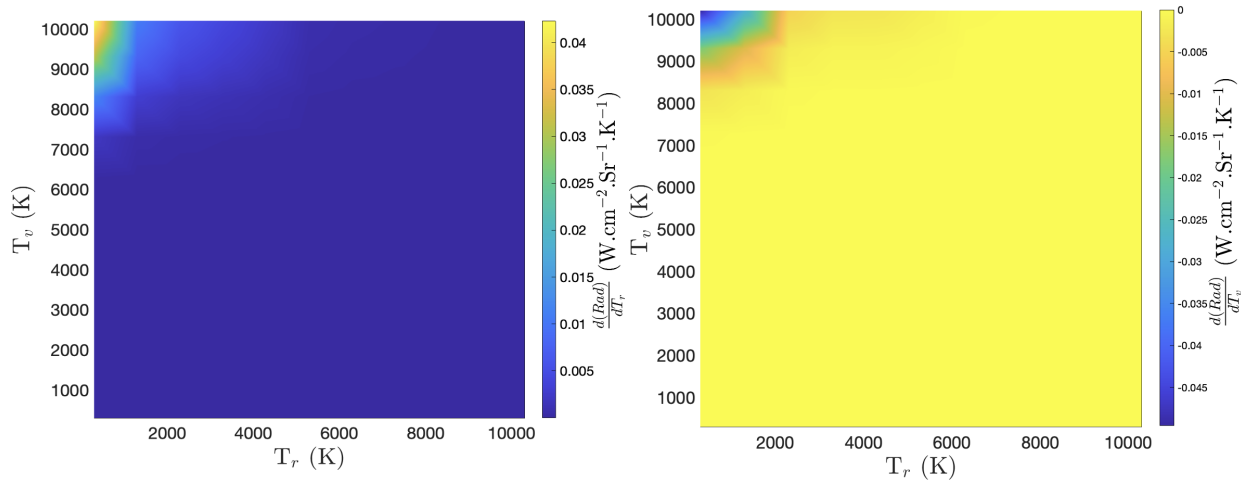


**Fig. 9 Sensitivity of total radiance between 380 and 700 nm for different temperatures.**

Another assumption to note regarding the optical depth is that the spectral radiance was simulated for an optically thin flow, which could lead to spectral radiance over-predictions from simulations if the flow is partially self-absorbing.

### C. Equilibrium assumption

Despite the transient nature of the flow, NEQAIR simulations were ran using the thermal-equilibrium number densities from CEA at each point along the line of sight corresponding to local  $T_r$ , to which a range of  $T_v$  profiles were fitted. All simulations generated are therefore expected to vary from the actual experimental spectra where  $T_r \neq T_v$  and the chemical composition of the gas is different to thermochemical equilibrium composition.

### D. Spectral fitting

For each discrete location along the centreline of the test section, the experimental spectra was fit to all simulations using a least-square routine, and the closest match kept to infer temperatures. An example of experimental spectra is shown in Fig 10, and corresponding simulations used for the fit in Fig 11. Band fitting was performed for the entire wavelength range, as well as for each wavelength subset.

The temperatures obtained by fitting subsets of the same spectra to simulations are weighted using their residuals to take into account how far they deviate from experiment, i.e how trust-worthy the fit is. Despite their lower signal-to-noise ratio, spectral fittings above 600 nm had consistently residuals orders of magnitude smaller than fittings under 500 nm. Spectral data under 500 nm was therefore discarded in the first stage of the fitting routine to ensure a more accurate estimation. Experimental relative magnitudes of the features in the lower wavelength range varied largely from simulations. Fig 10 shows bands between 350 and 500 nm of radiance comparable to emissions between 290 and 350 nm. Throughout all simulations generated using all combinations of input  $T_v$  and  $T_r$ , spectral radiance between 400 and 500 nm was orders of magnitudes smaller than below 400 nm, which can be seen in Fig 11. This discrepancy in

relative magnitudes made it harder to fit the data in this region using a least-square routine, as neighbouring spectral features could not be picked up by the routine due to their relative magnitude mismatch. Lowest residuals would be attributed to simulations of similar average intensity and divergence to the experiment, disregarding spectral features shapes. Reducing wavelength range of simulations also allowed finer resolution with smaller steps in  $T_v$  and  $T_r$ .

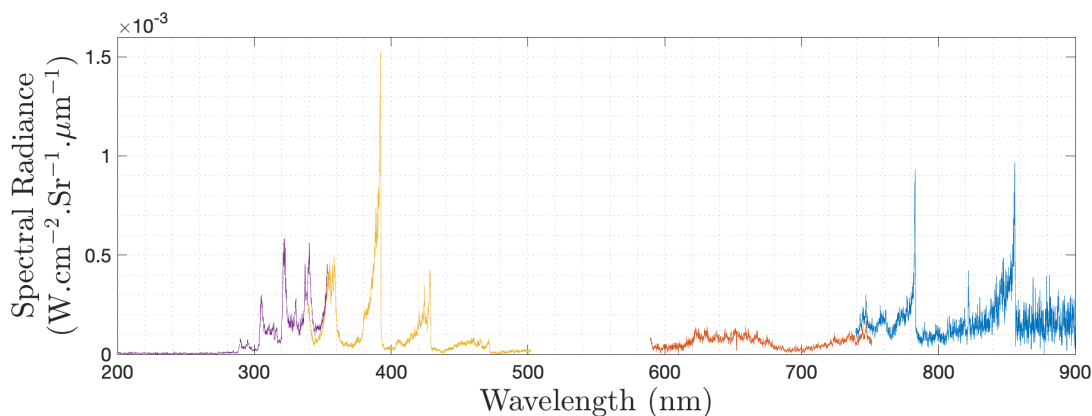


**Fig. 10** Example of  $N_2$  spectra at the nozzle exit. Lines under 500 nm have stronger magnitude than expected from simulation. Spectra were recorded from right to left (blue, orange, yellow, purple).

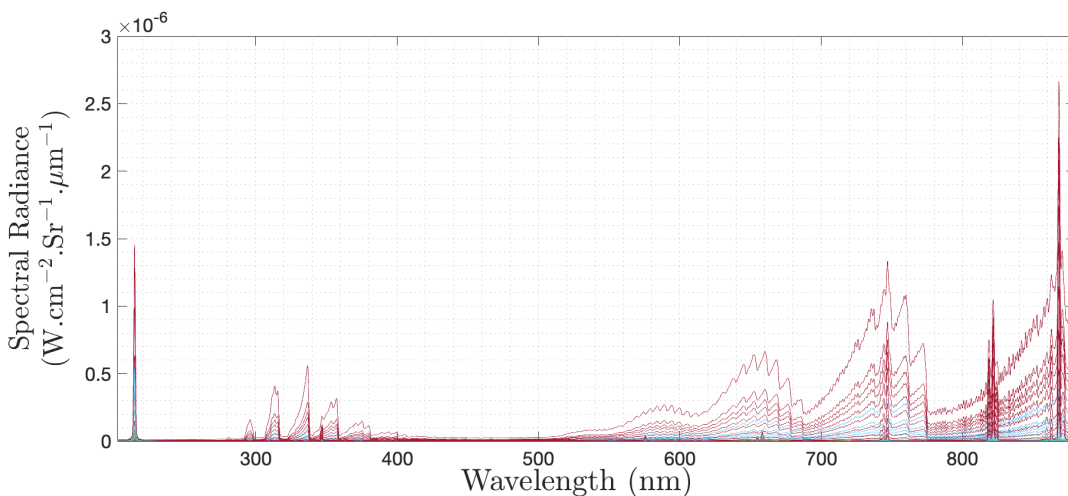


**Fig. 11** Example of  $N_2$  NEQAIR spectral radiance simulations for one spatial location (here at the nozzle exit). Simulations shown correspond to all combinations of  $T_v$  and  $T_r$  from 2300 to 10300 K.

An example of spectral fitting between experimental and numerical simulations using the higher wavelength spectral region is shown in Fig 12. Molecular nitrogen bands between 600 and 750 nm provided a good fit to the simulations, while the fitting routine had more difficulty to detect atomic lines due to the lower signal-to-noise ratio, and lower residuals would be attributed to the spectra with the closest average radiance. Within the reduced subset of 600 to 900 nm, narrower subsets were used to alleviate this issue and simplify the fitting of specific features. The output temperatures of each subsets were weighted using fits residuals.

To confirm the overall trend of spatial temperatures evolution obtained from the least-square routine fit, experimental spectra below 500 nm was loaded in LIFBASE for each location and the temperature outputs from the band fitting routine used to superimpose a simulated spectra. This also allowed fine-tuning of temperature outputs from the fitting routine: the high signal-to-noise ratio of the experimental spectra between 350 and 500 nm (yellow spectra in Fig 10) allows a finer manual fitting of spectral features, such as the well resolved  $N_2^+$  first negative system shown in Fig 13.

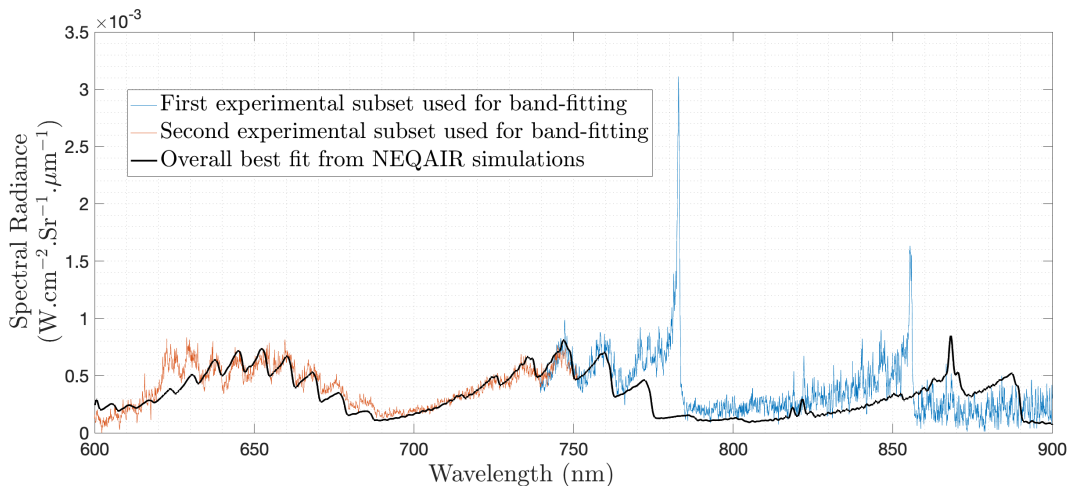


**Fig. 12** Example of  $N_2$  spectra at the nozzle exit with overall best fit between 600 and 900 nm. Fitted simulation corresponds to  $T_v = 4300$  K and  $T_r = 8400$  K.

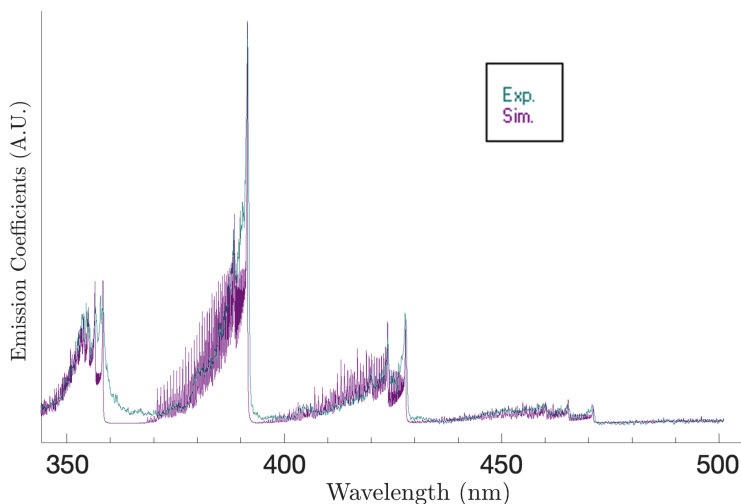


**Fig. 13** LIFBASE line fitting of the  $N_2^+$  B-X first negative system. Experimental spectra in green, simulated spectra generated using the least-square fitting routine output temperatures in purple. Best LIFBASE fit corresponded to  $T_v = 5200$  K and  $T_r = 8300$  K, both about 200 K higher than the original fit provided by the fitting routine and shown in Fig 12.

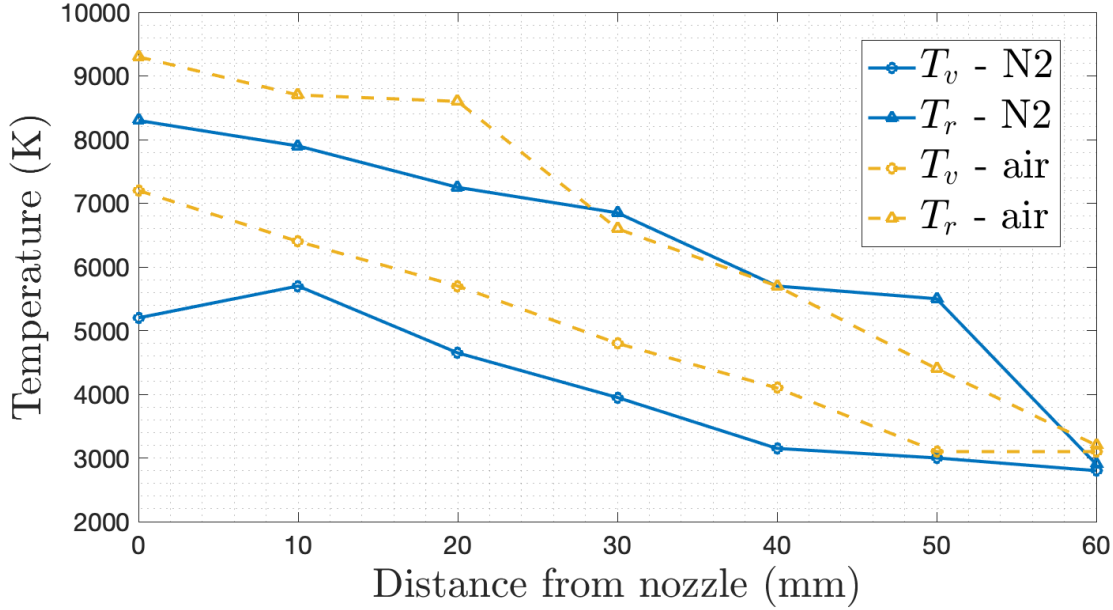
## VI. Results

Figure 14 shows the spatial temperature evolution of the  $N_2$  and air plasma for 250 A current and  $0.2 \text{ g.s}^{-1}$  mass flow rate.  $N_2$  flow was found to have a rotational temperature  $T_r$  varying from 8300 K at the nozzle to 2900 K 60 mm downstream, and vibrational temperature  $T_v$  varying from 5200 K to 2800 K. For the same operating conditions with air as test gas, rotational temperature  $T_r$  varied from 9300 K, and vibrational temperature  $T_v$  from 7200 K to 3100 K.

In both cases, rotational temperature was higher than vibrational temperature, and temperatures decreased as expected further downstream as the jet mixes with the colder chamber gas. Decrease in temperature was almost steady, apart from a small increase in  $T_v$  10 mm away from the nozzle for  $N_2$  flow. The gap between vibrational and rotational temperature decreased to only 100 K downstream in both cases, indicating that thermal equilibrium might be reached far from the nozzle.

In all cases, the temperatures obtained from the LIFBASE fit were higher than the ones obtained from the least-square routine, which could suggest that  $N_2^+$  molecules are at a higher temperature than the rest of the molecules. This could

also be due to a better fit quality, or to the fact the spectra used for LIFBASE fitting were recorded later during the runs, when the overall temperature in the chamber had probably increased, as explained in the following section.



**Fig. 14 Spatial temperature evolution of the jet.**

## VII. Discussion

Best fit for the same run were observed to differ between spectral ranges. This could be due to differences in signal-to-noise ratio between wavelength regions, or to the largely unsteady nature of the plasma, visibly varying over the duration of a run. As spectra were not recorded simultaneously for each spectral region, the flow characteristics could vary between two successive images captured, significantly if a singularity occurred during acquisition: copper lines were observed in the spectra, meaning that copper burnt during the experiment. This changed not only the composition of the gas, but also the shape of the plume. Moreover, the chamber pressure recorded during the run showed an increase over run duration, and we can assume that temperature overall increased with time: inferred flow temperatures were higher for air than for  $N_2$ , consistent with the fact that the transition from nitrogen to air flow was done later during the run. Spectra were recorded from higher to lower wavelength ranges, with about two minutes between successive image acquisitions required to adjust the spectrometer grating, the camera settings, and move long pass filters in and out of the optical path. This could explain the discrepancies in magnitudes observed between the different spectral regions of nominally same conditions: the spectra at lower wavelength corresponds to hotter test chamber temperatures. This is confirmed by the spectral radiance intensity an order of magnitude higher than expected from simulations at lower wavelength, for equal spectral radiance intensities at higher wavelengths. Likewise, temperatures from LIFBASE fittings were consistently higher than from the least-square fitting routine, which uses higher wavelength experimental spectra.

The decision to follow the same analysis for each spatial location by using the second spectra recorded (orange line in Fig 10, from 580 to 750 nm) for the fitting routine, and then refining temperature estimations in LIFBASE using the third recorded spectral region (yellow line in Fig 10, from 340 to 500 nm) avoids discrepancies due to time varying parameters between the different locations, as spectral regions are recorded at different times but are each resolved in space. Consequently, spectra from the same spectral region but at different spatial locations were generated from the same spatially-resolved image and moment in time.

The discrepancies between measured and simulated spectral radiance could also be caused by the various assumptions made during the analysis, such as assuming number densities at thermal-equilibrium to fit temperature profiles where  $T_v \neq T_r$ , the semi-empirical equation to compute enthalpy profiles, or the estimation of the jet diameter.

Finally, the least-square fitting routine did not always provide the best qualitative fit, and all fits had to be visually



examined to decide if subsets should be used. Residuals were sometimes lower for two spectra of different shapes but overall similar averages and variation magnitudes than for spectra following the same trends but separated by an offset. This type of fitting does not encapsulate the qualitative value of the spectra and does not make use of the finer distinctive features.

## VIII. Conclusion and Future Work

This paper discusses the development of a spectroscopy system and its integration to the new Oxford University arc-jet facility OPG2. The set-up is used to obtain spatially-resolved emission spectroscopy data to estimate temperatures of the core flow through band-fitting of experimental data to radiative simulations using a two-temperature model. For operating conditions of 250 A and  $0.2 \text{ g.s}^{-1}$ ,  $N_2$  flow was found to have a rotational temperature  $T_r$  varying from 8300 K at the nozzle to 2900 K 60 mm downstream, and vibrational temperature  $T_v$  varying from 5200 K to 2800 K. For the same operating conditions with air as test gas, rotational temperature  $T_r$  varied from 9300 K to 3000 K, and vibrational temperature  $T_v$  from 7200 K to 3100 K.

Due to experimental incentives, the calibration of the system was done after the tests. By improving the spatial focus, spatial smearing could be decreased further downstream and a larger portion of the field of view used to resolve temperature on a longer section along the centreline. As radiance depends on the optical path length, more work is necessary to assess the actual size of the jet. Future test campaigns will use high-speed imaging to perform Abel inversions and recreate a cross-section of the jet. Finally, the least-square routine used to fit the data does not emphasise band shape enough, and a more accurate fitting technique should be used in future analysis.

Future work will include performing emission and absorption spectroscopy in the VUV and UV regions of the spectrum respectively, by designing an insert able to be fully evacuated up to an embedded window located in the vicinity of the plasma jet.

## Acknowledgments

This research was funded by the UKRI Future Leaders Fellowship scheme (grant number MR/T041269/1), and we extend our gratitude to UKRI. For Open Access, the author has applied a CC BY public copyright licence to any Author Accepted Manuscript (AAM) version arising from this submission.

## References

- [1] Brandis, A. M., and Johnston, C. O., "Characterization of stagnation-point heat flux for earth entry," *45th AIAA Plasmadynamics and Lasers Conference*, 2014. <https://doi.org/https://doi.org/10.2514/6.2014-2374>.
- [2] Bose, D., McCorkle, E., Thompson, C., Bogdanoff, D., Prabhu, D., Allen, G., and Grinstead, J., "Analysis and Model Validation of Shock Layer Radiation in Air," *46th AIAA Aerospace Sciences Meeting and Exhibit*, 2008. <https://doi.org/https://doi.org/10.2514/6.2008-1246>.
- [3] Loehle, S., Zander, F., Eberhart, M., Hermann, T., Meindl, A., Massuti-Ballester, B., Leiser, D., Hufgard, F., Pagan, A. S., Herdrich, G., and Fasoulas, S., "Assessment of high enthalpy flow conditions for re-entry aerothermodynamics in the plasma wind tunnel facilities at IRS," *CEAS Space J*, Vol. 14, 2022, p. 395–40. <https://doi.org/https://doi.org/10.1007/s12567-021-00396-y>.
- [4] Laux, C. O., Spence, T. G., Kruger, C. H., and Zare, R. N., "Optical diagnostics of atmospheric pressure air plasmas," *Plasma Sources Science and Technology*, Vol. 12, No. 2, 2003, pp. 125–138. <https://doi.org/10.1088/0963-0252/12/2/301>.
- [5] Hermann, T., Löhle, S., Fasoulas, S., Leyland, P., Marraffa, L., and Bouilly, J.-M., "Influence of Ablation on Vacuum-Ultraviolet Radiation in a Plasma Wind Tunnel Flow," *Journal of Thermophysics and Heat Transfer*, Vol. 31, No. 3, 2017, pp. 575–585. <https://doi.org/10.2514/1.T4936>.
- [6] Hermann, T., and Chang, E. W. K., "Optical Temperature Measurement in Unsteady Plasma Free Jet," *Measurement Science and Technology*, 2024. Submitted for Review.
- [7] Chang, E. W. K., Valeinis, O., Schäfer, J., Buquet, M. T. B., and Hermann, T. A., "Commissioning the OPG1 Plasma Wind Tunnel," *34th International Symposium on Shock Waves*, 2023, p. 1–10.
- [8] Schäfer, J., Chang, E. W. K., Hermann, T. A., and Löhle, S., "Experimental Investigation of a Small-Scale Arc-Jet for Earth Entry Simulation," *AIAA SciTech 2024 Forum*, 2023.

- [9] Valeinis, O., Chang, E. W. K., and Hermann, T. A., "Development and Testing of Slug Calorimeter and Total Pressure Probes for a Miniaturized Arc-jet," Vol. AIAA SciTech 2024 Forum, 2023.
- [10] Luis, D., and Macdonald, M. E., "Emission Spectroscopy Characterization of Electrodes Species in the Freestream Flow at the NASA Ames Miniature Arc Jet II Facility," *Journal of quantitative spectroscopy and radiative transfer*, Vol. 272, 2021. <https://doi.org/https://doi.org/10.1016/j.jqsrt.2021.107752>.
- [11] Chang, E. W. K., Joglekar, C., McGilvray, M., and Hermann, T. A., "Integration of Arc-jet in Impulse Facility for Hypervelocity Aerothermal Testing with Ablation," *AIAA SciTech 2023 Forum*, 2023. <https://doi.org/10.2514/6.2023-2334>.
- [12] Hermann, T. A., Chang, E. W. K., Schäfer, J., Joglekar, C., and Böhrk, H., "Development of Small Scale Arc-jet Facility OPG1," *AIAA SciTech 2023 Forum*, 2023, pp. 1–24.
- [13] Buquet, M. T. B., Glenn, A., Collen, P., Williams, B., McGilvray, M., and Hermann, T., "Design of a Spatially Resolved VUV Spectroscopy System for Shock Tube Flows," *9th International Workshop on Radiation of High Temperature Gases*, 2022.
- [14] Greenberg, R. B., Cruden, B. A., Grinstead, J. H., and Yeung, D., "Collection optics for imaging spectroscopy of an electric arc shock tube," *Novel Optical Systems Design and Optimization XII*, Vol. 26, No. 74290H, 2009.
- [15] Yury, "Optometrika," *Github*, 2002.
- [16] Cruden, B. A., "Absolute Radiation Measurements in Earth and Mars Entry Conditions," 2014.
- [17] Fasoulas, S., Sleziona, P. C., Auweter-Kurtz, M., Habiger, H. A., Laure, S. H., and Schoenemann, A. T., "Characterization of a Nitrogen Flow Within a Plasma Wind Tunnel," *Journal of Thermophysics and Heat Transfer*, Vol. 9, No. 3, 1995, pp. 422–431. <https://doi.org/https://doi.org/10.2514/3.684>.
- [18] Luque, J., and Crosley, D., "LIFBASE: Database and Spectral Simulation Program," 1999.